1 **Interaction between typhoon, marine heatwaves, and internal tides:**
2 **Observational insights from Ieodo Ocean Research Station in the northern**
3 **East China Sea**

4 **J. S. Saranya[1], Panini Dasgupta[2]† and SungHyun Nam[1, 3]**

5 *[1]School of Earth and Environmental Sciences, College of Natural Sciences, Seoul National*

6 *University, Seoul, Republic of Korea*

7 *[2]Future Innovation Institute, Seoul National University, Siheung 15011, Republic of Korea*

8 *[3]Research Institute of Oceanography, College of Natural Sciences, Seoul National University,*

9 *Seoul, Republic of Korea*

10 Corresponding author: Panini Dasgupta (panini@snu.ac.kr)

11

12

13 **Key Points:**

14 • Typhoon Hinnamnor (2022) re-intensified after interacting with underlying Marine
15 Heatwave (MHW) in the East China Sea.

16 • Typhoon wind-driven mixing dissipated the underlying MHW.

17 • Stratification change induced by the typhoon altered the local generation site of
18 semidiurnal internal tides, thereby reducing its activity.

19 **Abstract**

20 Typhoons, fueled by warm sea surface waters, heighten concern as they increasingly interact with
21 frequent Marine Heatwaves (MHWs) in a changing climate. Typhoon Hinnamnor (2022)
22 weakenned and re-intensified as it approached the Korean Strait, interacting with underlying
23 MHW in the northern East China Sea (nECS). Here, we found a substantial increase in latent heat
24 loss from the nECS during the MHW period, contributing to the typhoon re-intensification from
25 in-situ observations supplemented by reanalysis products. Strong sea surface wind forcing
26 associated with the typhoon enhanced vertical mixing and upwelling, resulting in a pronounced
27 (0.90°C) sea surface cooling after the typhoon passage, facilitating MHW dissipation with reduced
28 thermal stratification. Such changes in background stratification, furthermore, significantly
29 weakened semidiurnal internal tides due to unfavorable condition for generation from a nearby
30 source. These findings underscore the importance of continuous time-series observations for
31 monitoring interaction processes among the extremes in a changing climate.

32 **Plain Language Summary**

33 Typhoons, powered by warm ocean waters, are causing more concern as they increasingly interact
34 with frequent episodes of extremely warm sea conditions known as Marine Heatwaves (MHWs)
35 in our changing climate. This study focuses on Typhoon Hinnamnor in 2022, which went through
36 a weakening and strengthening cycle as it neared the Korean Strait and encountered an MHW in
37 the northern East China Sea (nECS). By using in-situ data collected in the nECS and additional
38 data analysis, we discovered a significant increase in heat loss from the nECS during the MHW,
39 contributing to the typhoon getting stronger again. The powerful winds from the typhoon caused
40 enhanced mixing and cooling of the sea surface after it passed, helping to dissipate the MHW and
41 reduce the layering of temperatures in the ocean. We also observed changes in temperature patterns
42 during and after the MHW, emphasizing the importance of ongoing observations to understand
43 and monitor these interactions in our changing climate.

44 **1. Introduction**

45 The northwestern Pacific region is the most favorable globally for typhoon development,
46 generating over a third of all typhoons annually, with an average of 16 typhoons forming and
47 traversing the area each year, roughly twice the number of Atlantic hurricanes (Gray, 1968; Chen
48 & Ding, 1979; Webster et al., 2005). Projections suggest that warming climate has led to an
49 increase in typhoon intensity and destructive potential, supported by observations (Murakami et
50 al., 2020) and climate model simulations (Chu et al., 2020), also resulting in a notable rise in
51 extreme events like powerful typhoon storm surges (Knutson et al., 2019) and Marine Heatwaves
52 (MHWs) (Hobday et al., 2016; Saranya et al., 2022; Saranya and Nam, 2024; Dasgupta et al.,
53 2024). These pose a significant threat to marine and coastal ecosystems worldwide, as well as to
54 the sustainable development of coastal economies and societies (Emanuel, 2003; Jin et al., 2014;
55 Emanuel, 2013; Bindoff et al., 2019; Collins et al., 2019; Oppenheimer et al., 2019).

56 The East China Sea (ECS), a partially enclosed marginal sea in the northwestern Pacific, features
57 a broad continental shelf with shallow water depths, typically <100 m. The ECS features unique
58 dynamical characteristics, including the generation of semidiurnal internal tides (ITs) facilitated
59 by the Okinawa trough to the south of the northern ECS (Lee et al., 2006; Zhao, 2014; Xu et al.,
60 2016; Cho et al., 2016; Nam et al., 2018; Lee and Nam, 2021). These ITs, arising from barotropic
61 tidal currents flowing over abrupt ocean bottom topography, play a crucial role in the region's

62 ocean dynamics, alongside locally generated ITs on the shelf (Eich et al., 2004). Therefore, the
63 ECS poses distinctive dynamical characteristics that produce a complex background condition
64 during the occurrences of extremes such as typhoons and MHWs. Moreover, the ECS is
65 experiencing a warming trend significantly higher than the global average (Cai et al., 2017; Yan
66 et al., 2020), leading to the emergence of strong and prolonged MHWs (Gao et al., 2020; Dasgupta
67 et al., 2024). While most northwestern Pacific typhoons decay over the ECS region, a warming
68 climate has led to increased interactions between typhoons and the rapidly warming ECS, resulting
69 in their re-intensification rather than decay. Typhoons undergo unique intensification in coastal
70 regions, affecting sea surface temperatures (SST) (Jacob et al., 2000; Emanuel, 2003; Zheng et al.,
71 2010b) and oceanic processes like vertical mixing and thermocline shoaling (Zheng et al., 2010;
72 Lin et al., 2011; Balaguru et al., 2012; Nam et al., 2012; Wada et al., 2014; Park et al., 2019;
73 Kawakami et al., 2022; Kang et al., 2024). Understanding these complex interaction processes
74 among extreme events such as typhoons, MHWs, and ITs is crucial for enhancing our capabilities
75 to forecast extremes and mitigate their destructive impacts. While previous studies have addressed
76 how typhoons intensify in the presence of MHWs and consequently how MHWs decay (Rathore
77 et al., 2022; Pun et al., 2023), the effects of these interactions on the ocean's background
78 thermodynamic conditions have yet to be further explored.

79 Typhoon Hinnamnor, originating in the northwestern Pacific on 28 August, 2022, intensified into
80 a super typhoon upon entering the nECS between 3–5 September , reaching a maximum wind
81 speed of 46.3 m s^{-1} amid existing MHW conditions. After causing significant damage upon making
82 landfall in the Korean Peninsula on 6 September, 2022, Hinnamnor transitioned into an
83 extratropical cyclone upon entering the East Sea (Japan Sea). The typhoon Hinnamnor passed over
84 two continuous in-situ observation facilities, the Ieodo Ocean Research Station (I-ORS, 125.10°E,
85 32.07°N) and the Jeju Numbu Buoy (JNB, 126.15°E, 32.03°N), which recorded the interaction
86 between the two extremes and provide a unique opportunity to study the interaction in high
87 temporal resolution. This study presents the first comprehensive analysis of critical ocean-
88 atmosphere interactions during the typhoon's re-intensification amidst MHWs and the subsequent
89 dissipation of MHWs in the nECS, alongside variations in ITs patterns at the I-ORS due to changes
90 in background stratification, independent of external (barotropic) tidal forcing.

91 **2. Data**

92 **2.1.1. In-situ time series and hydrographic data**

93 Typhoon Hinnamnor passed through the Korea Strait in the vicinity of time-series observation
94 sites of I-ORS and JNB, both located in the nECS (Figure 1a, b and c). We used the meterological
95 observations, including wind speed, direction, air temperature, and relative humidity at 42.3 m
96 above mean sea level, as well ashydrographic observations comprising in-situ temperatures and
97 salinities measured at depths of 3, 21, and 38 m from the I-ORS.   Additionally, we incoorporated
98 wind speed, direction, air temperature, relative humidity at a 10 m height, SST and sea surface
99 salinity from the JNB buoy. Detailed information regarding the time-series observations from I-
100 ORS and JNB is provided in supplementary Table S1.
101 Furthermore, bi-monthly (from 19–23 August 2022) ship-based hydrographic observational data
102 (National Institute of Fisheries Science (NIFS)) from 32 stations (Lines 315, 316, and 317) in the
103 nECS were utilized (Figure 1a, b, c). It includes both water temperature and salinity at 0, 10, 20,
104 30, 50, 75 m water depths. All observational data used in this study have undergone standard

quality control and quality assurance procedures (UNESCO/IOC ocean data standards). Derived parameters like potential temperature, practical salinity, and potential density are calculated using the Thermodynamic Equation of SeaWater 2010 (TEOS-10) toolbox.

2.1.2. Other data products

Since meteorological parameters are observed at a height of 42.3 m at I-ORS, we also used Modern-Era Retrospective analysis for Research and Applications, Version 2 (MERRA-2) (1980-present). This involved analyzing surface fluxes, wind speed, relative humidity, and air temperature at a 10 m height (standard height to estimate flux parameters), with a time interval of 1 hr and horizontal resolutions of 0.5° latitude × 2/3° longitude (Gelaro et al., 2017). We used the bathymetric slope derived from NOAA National Centers for Environmental Information. 2022: ETOPO 2022 16 Arc-Second Global Relief Model for the slope analysis. We used potential temperature, salinity from Global Ocean Physics Analysis and Forecast data with 0.083° × 0.083° spatial resolution and 6 hr temporal resolution to find out the buoyancy frequency for the IT generation site analysis. The credibility of the Global Ocean Physics Analysis and Forecast data has been extensively verified with the I-ORS in-situ observation and the ship-based hydrographic observations. To identify surface MHW, we used daily SST data from the Optimum Interpolated SST (OISST) dataset with a spatial resolution of 0.25° × 0.25° for the period 1982–2018 (Reynolds et al., 2007).

2.2. Methods

The position and pressure of typhoon center, and maximum wind speed of typhoon Hinnamnor were calculated in 3 hr intervals by linearly interpolating the 6 hr best track data (Kunitsugu, 2012). The typhoon's displacement was then determined every 3 hr, and the translation speed was defined as the displacement divided by 3.

Efficient heat transfer from the ocean to the atmosphere is a fundamental process in typhoons (Malkus and Riehl 1960; Emanuel 1986). Obtaining direct measurements of turbulent fluxes in typhoons, particularly under high-wind conditions, is challenging (Drennan et al. 2007; Zhang et al. 2008). Therefore, we rely on parameterizations, with heat and moisture fluxes commonly described using bulk aerodynamic formulas. These formulas depend on easily measurable near-surface atmospheric and upper-ocean data (e.g., Shay et al. 2000; Shay and Uhlhorn 2008; Shay 2010; Jaimes et al. 2015, 2016) as follows. $Q_s = \rho_a c_p C_h U_{10}(\text{SST} - T_a)$, $Q_l = \rho_a L_{vap} C_q U_{10}(q_s - q_a)$ where Q_s and Q_l denote the bulk air–sea sensible and latent heat flux, respectively (the total flux is defined as $Q_s + Q_l$). The ρ_a, c_p and L_{vap} represent atmospheric density, specific heat capacity of air at constant pressure (1004 J kg^{-1} °C^{-1}), latent heat of vaporization (2.5 × 10^6 J kg^{-1}) respectively. C_h and C_q are surface exchange coefficients as 1.1 × 10^{-3} $((0.7375 + 0.0525 U_{10}) \times 10^{-3}$ for 5 m s^{-1} $\leq U_{10} < 25$ m s$^{-1}))$, $C_h = C_q$ (Jaimes et al., 2015) of sensible and latent heat, respectively, U_{10} is the 10 m wind speed, T_a is the 10 m air temperature, q_s is the saturated specific humidity at the SST (hypothesized as at 98% saturation at the SST) (Buck. 1981) and q_a is the 10 m atmospheric specific humidity. Additionally, $\Delta T = \text{SST} - T_a$ and $\Delta q = q_s - q_a$ correspond to the air-sea temperature and moisture differences, collectively referred to as thermodynamic disequilibrium. We used wind speed, T_a, and relative humidity from I-ORS at 42 m and the 3 m temperature at I-ORS is considered as SST.

149 We calculated the Ocean Heat Content (OHC) using temperature profiles at I-ORS as follows

150 $OHC = \rho_w c_p \int_{D_{38}}^{0} T - T_{min} \, dz$. The ρ_w, c_p, D_{38}, T_{min}, represent the average sea water density

151 (1029 kg m^{-3}), specific heat capacity of seawater, maximum observation depth at I-ORS and

152 minimum temperature from the observation respectively. To delineate the role of stratification we

153 derived the squared buoyancy frequency (N^2) as, $N^2 = -\frac{g}{\rho_0}\frac{\partial \rho}{\partial z}$ where, g, ρ_0, ρ represent the gravity

154 constant (9.8 m s^{-2}), backgraound density (1,025 kg m^{-3}) and potential density at I-ORS derived

155 from potential temperature. At I-ORS, the Mixed Layer Depth (MLD) is defined as the depth

156 where the temperature changes by 0.8°C from the temperature measured at 3 m depth.

157 Fast Furier Transform band-pass filter with cutoff periods of 8 and 16 hr was used to extract the

158 semidiurnal fluctuations from the time-series of sea level, potential temperature and potential

159 density. To determine the dominance of the main tidal components, especially the semidiurnal

160 major constituents M_2 and S_2, we computed the tidal amplitude and phase of sea level records.

161 This was done using the harmonic analysis method described by Pawlowicz et al. (2002) and

162 implemented through a Matlab toolbox (Harmonic analysis of time series using Least Square Fit,

163 M MA, 2024).

164 We relied on the linear theory that the internal tides tend to form under optimal circumstances

165 when the slope of the seabed (S) aligns closely with the characteristic slope of the waves, C=$\pm$

166 $\sqrt{\frac{(\omega^2 - f^2)}{(N(z)^2 - \omega^2)}}$, where ω, f, N, and z are the wave frequency, inertial frequency, buoyancy frequency,

167 and the vertical coordinate (Knauss and Garfield 2016). In such scenarios, the orientation of the

168 tidal ellipse across the continental shelf becomes significant for facilitating internal tide generation

169 (Holloway et al., 2001).

170 **3. Results**

171 **3.1. Timeline of typhoon Hinnamnor-MHWs interaction and accoiated air-sea exchanges**

172 In this section, we explain the timeline of the interaction between typhoon Hinnamnor and MHWs,

173 along with the associated air-sea processes as recorded at I-ORS. A moderate category MHW was

174 identified in the nECS, commencing on 23 August, 2022, at the I-ORS location and persisting until

175 4 September, 2022 with a lifespan of 13 days (Figure 1 c). We define this period as P1 specifying

176 the MHWs period. The SST anomaly peaked on 30 August, surpassing 3°C, with a cumulative

177 intensity of 373.53°C day (Figure 1a and c). Typhoon Hinnamnor, originating on 28 August,

178 along-track time series of the typhoon's central pressure exhibited a double peak in its life cycle,

179 indicating two intensification phases. This typhoon encountered large-scale MHW upon entering

180 the nECS on 4 August, covering most of the region in nECS, with a central pressure of 950 hPa

181 (Figure 1a). From 21:00 UTC 4 September (hereafter, all time information is presented in UTC),

182 the typhoon's central pressure started decreasing, reaching 940 hPa by 5 September. During 4–6

183 September, the typhoon's wind speed increased by 5.14 m s^{-1} within 24 hr after the interaction with

184 underlying MHWs at the nECS. At the I-ORS location, MHWs were present until 4 September

185 with SST anomaly 1.5°C. The MHW anomaly dissipated abruptly by 5 September after

186 encountering the approaching typhoon winds (Figure 1b and c). We define this period from

187 September 4 to 5 as P2 when typhoon interacted with underlying MHWs at the I-ORS location
188 and diminished it.

189 On 4 September the MHW dissipated, and Hinnamnor reintensified subsequently. At I-ORS, wind
190 speed and wave height surged as typhoon Hinnamnor approached on September 4–5, reaching
191 maximum of 30 m s^{-1} and 8–10 m respectively on 6 September (Figure 2a, b, c, and d). Overall,
192 typhoon winds were present at the I-ORS location during 4–7 September. We define this period
193 as P3, partially overlapping with the earlier defined period P2. Typhoon winds peaked at I-ORS
194 location during 6 September. We divide P3 into periods before and after the peak wind intensity
195 as $P3_1$ and $P3_2$, respectively. During P1, SST and the temperature at 3 m were higher than air
196 temperature, but by 1 September, air temperature surpassed SST. During the typhoon-MHW
197 interaction (P2), latent and sensible heat fluxes from ocean to atmosphere increased (reaching upto
198 50 kJ m^{-2} & 20 kJ m^{-2} , respectively) and subsequently air temperature increased by 2°C. After 4
199 September, both SST and 3 m temperature dropped. JNB data and MERRA-2 also show a
200 consistent variability as observed in I-ORS (Figure S1a and b). Shortwave radiation was high
201 during the late August (300–500 kJ m^{-2}) during the genesis and intensification of MHWs (P1
202 period) and significantly reduced during typhoon passage ($P3_1$) (Figure 2f). We define the post
203 typhoon passage at I-ORS from 7–14 September as P4 (Figure 2).

3.2. Changes in ocean interior environment before, during and after typhoon passage

205 The ocean underwent significant changes before, during, after the interaction between the MHW
206 and typhoon Hinnamnor. From late August to 4 September (P1), surface waters were warm (26–
207 28°C), less dense, and less saline, while cooler, denser, and more saline water existed below 20 m.
208 During the typhoon passage ($P3_1$ and $P3_2$), temperatures in the upper 20 m decreased, and
209 upwelling of colder water occurred below 30 m ($P3_2$) upper layers (0-20 m) became homogeneous
210 with 24°C, whereas ocean temperature became 16 °C below 30 m depth (Figure 3a). Post-typhoon
211 (P4), upper surface gained heat due to increased solar influx and, resulting in increased SST
212 (Figure 2a). Also upper water column became less denser due to fresh water flux during the
213 typhoon passage (Figure 2b). Vertical profiles indicated a deepening of the MLD by 20 m from
214 21:00 5 September to 06:00 6 September, 2022 ($P3_1$ to $P3_2$) during the typhoon passage (Figure
215 2g). Temperature, density, and salinity profiles during different stages like P2, $P3_1$, $P3_2$ and P4
216 showed a homogeneous upper surface with cold, less dense, and less saline water, indicating the
217 existence of a well-mixed surface layer with cold subsurface layers. Additionally, temperature
218 decreased by 1.32°C on the surface after P2, with mixing at the upper 20 m and upwelling at 38 m
219 (temperature decreased by 1.39°C). Furthermore, during P4, temperatures decreased by 2.73°C
220 compared to 29 August 2022 (P1).

221 During the MHW (P1), significant fluctuations in isotherms, isopycnals, and isohalines occurred
222 at mid-depths in I-ORS, which diminished following the typhoon passage from 9–17 September
223 despite of the barotropical tidal forcing (Figure 3). OHC at the upper 38 m exhibited high values
224 with oscillations during the MHW period (P1), decreasing during the MHW-typhoon interaction
225 (P2) and significantly reducing post-typhoon passage (P4), reaching around 1×10^9 kJ m^{-2} (Figure
226 2d). During the MHW period (P1), stratification at 12 m depth exhibited enhanced oscillations,
227 followed by a decrease during the typhoon, and increased stratification from 9–17 September (P4).
228 Conversely, at 29 m depth, fluctuations increased during the MHW period, followed by a decrease
229 and maintenance during the typhoon (P2, $P3_1$, $P3_2$) and post-typhoon period (Figure 3e). Tidal

230 harmonic analysis of sea level data at I-ORS and spectral analysis of temperature at 3, 21, and 38
231 m revealed barotropic spring tides during 28 August to 1 September (P1) and after the typhoon
232 passage from 10 September to 17 September (P4), while neap tides were present during the
233 typhoon passage at I-ORS (P2, $P3_1$ and $P3_2$) (Figure S2a, 3f). Periodicity spectral analysis of
234 temperature before (28 August to 5 September) (P1) and after (9–17 September) (P4) the typhoon
235 passage confirmed the presence of ITs with a periodicity of 12.4 hr. The 8–16 hr bandpass filtered
236 time series of isotherm displacement (18, 20, and 22°C) and N^2 exhibited enhanced oscillations
237 during the MHW period from 28 August to 2 September (P1), coinciding with the barotropic spring
238 tidal cycle (Figure S2c, f). After the typhoon passage from 9–17 September (P4), despite the
239 spring barotropic forcing, there were reduced isotherm displacement and N^2 oscillations (Figure
240 S2c, f).

241 In order to investigate the changes in the ITs we relied on the Global Physical Analysis forecast
242 data. Time-depth evolution of potential temperature, potential density, practical salinity, and 8–16
243 hr bandpass filtered potential density from both the I-ORS location and the Global Physical
244 Analysis forecast data from 28 August to 17 September, 2022, show the model effectively captures
245 the MHW presence and typhoon-induced vertical mixing and wind curl-driven upwelling (Figure
246 S3 a-g). However, it fails to reproduce the IT fluctuations observed in isotherms, isopycnals, and
247 isohalines also visible in the bandpass filtered potential density (Figure S3 d and h). Additionally,
248 warm bias in the upper layer >20 m is noted after the typhoon passage in the model, where a
249 constant temperature of 25°C is present (Figure S3 a and b). Comparisons between NIFS shipboard
250 hydrographic observations and model zonal sections during 19–23 August 2022 further confirmed
251 the model's performance, with biases ranging from -0.9–0.9 for potential temperature, potential
252 density, and practical salinity (Figure S4). Hence, using the model's physical variables, changes in
253 stratification and the generation site of ITs were explored.

254 The passage of typhoon Hinnamnor induced vertical mixing and wind-driven upwelling, resulting
255 in a significant decrease in stratification post-passage (Figure 3e) and reducing semidiurnal
256 isotherm fluctuations.The spatial distribution of N^2 which enhanced and oscilated during
257 MHWfrom 28 August to 4 September (P1), with values >0.0012 s^{-2} pre-typhoon passage,
258 decreasing to 0.0006–0.0011 s^{-2} during the typhoon passage (4–6 September) ($P3_1$), and further
259 decreasing from 9–17 September (P4), particularly around the I-ORS location and most regions in
260 the nECS (Figure 4a, b, c). We observed a generation site for ITs near the I-ORS and JNB which
261 is evident from the spatial map of C-S, where the near zero values of C-S depicts the generation
262 site region. The identified generation site has a slope ranging from 0.005–0.0065 (Figure S6 b).
263 Consequently, enhanced IT oscillations were observed at the I-ORS location alongside spring tidal
264 forcing. However, during and after the typhoon passage, stratification reduced at the I-ORS and
265 nearby places, with C increasing to 0.0055–0.0065 (C-S>0), leading to reduced generation of ITs
266 despite spring tidal forcing (Figure 4 d, e, and f).

4. Discussions and Conclusions

268 The in-situ time-series observations from two fixed locations of I-ORS and JNB captured a
269 detailed interaction between the two extremes, typhoon Hinnamnor and MHW and provided a
270 unique opportunity to study the interactions between these two extremes. This study explains how
271 typhoon reintensified after interaction with the underlying MHW and how the ocean conditions
272 impacted by these extremes. Previous research, such as the study on typhoon Bavi (2020) in the

nECS, has highlighted the role of MHWs, where SST exceeding 30°C fueled typhoon intensity, while subsiding airflows away from typhoon zones, coupled with intense solar radiation, often lead to rapid warming of SST, potentially affecting typhoon landfall intensity (Lok et al., 2021; Pun et al., 2023). Typhoon Hinnamnor experienced reintensification with a wind speed increase of 5.14 m s^{-1}, and in-situ observations from I-ORS indicated that typhoon winds induced a latent heat release (50 kJ m^{-2}) from the ocean to the atmosphere, resulting in a 1.92°C decrease in temperature at 3 m during the MHW-typhoon interaction compared to 29 August to 4 September. Studies have consistently demonstrated that the primary catalyst appears to be an MHW, contributing a significant surplus of heat flux that typhoons would not typically encounter in normal conditions (Rathore et al., 2022; Pun et al., 2023; Choi et al., 2024).

In addition to explaining the reintensification of typhoon by MHW this study presents the subsequent demise of MHW by typhoon. Notably, the study observes amplified and reduced ITs during the MHW and post-typhoon periods, respectively, despite both corresponding to the barotropic spring tide. The observed changes in ITs in the nECS are linked to typhoon-induced alterations in stratification. This research aligns with previous findings that demonstrated the significant impact of typhoon winds, as seen with Chanhom and Nangka in July 2015, rapidly transforming ocean conditions along southeast coast of Korea and influencing ITs during downwelling events. This underscores the potential for typhoons to induce distinctive coastal environmental changes (Chae et al., 2021).

This study reports, for the first time, the possible generation site of ITs in the nECS near the I-ORS and JNB. Unlike prior studies focusing on MHW-typhoon dynamics, our research unveils unprecedented oceanic changes arising from the interaction of these extreme events, a previously undocumented aspect. The existence of MHW and favorable stratification conditions supported local IT generation, manifesting in strong isothermal oscillations at the I-ORS. Following typhoon-induced stratification changes, the generation site ceased to exist, leading to a reduction in isothermal oscillations at the I-ORS (Figure 4j). The study underscores the importance of long-term ocean observations for understanding interactions between ocean extremes and emphasizes the significance of studying ITs for energy distribution within the ocean.

Acknowledgments

316 This work is also partially funded by KHOA through the application program of Ieodo Ocean
317 Research Station.

318
319 **Open Research**

320

321 **References**

322 Balaguru, K., Chang, P., Saravanan, R., Leung, L. R., Xu, Z., Li, M., & Hsieh, J. S. (2012). Ocean
323 barrier layers' effect on tropical cyclone intensification. *Proceedings of the National Academy of*
324 *Sciences*, 109(36), 14343-14347.

325
326 Bindoff, N. L., Cheung, W. W. L., Kairo, J. G., Arístegui, J., Guinder, V. A., Hallberg, R., et al.
327 (2019). Changing ocean, marine ecosystems, and dependent communities. *In IPCC Special Report*
328 *on the Ocean and Cryosphere in a Changing Climate*, 477-587.

329
330 Cai, R., Tan, H., & Kontoyiannis, H. (2017). Robust surface warming in offshore china seas and
331 its relationship to the east asian monsoon wind field and ocean forcing on interdecadal time scales.
332 *Journal of Climate*, 30(22), 8987–9005. https://doi.org/10.1175/jcli-d-16-0016.1

333
334 Chae, J. Y., Jeon, C., Kim, P., Hirose, N., Ku, A., & Park, J. H. (2021). Variation of semidiurnal
335 internal tides along the southeastern coast of korea induced by typhoons. *Journal of Marine*
336 *Science and Engineering*, 9(3), 328.

337
338 Cho, C., Nam, S., & Song, H. (2016). Seasonal variation of speed and width from kinematic
339 parameters of mode-1 nonlinear internal waves in the northeastern east china sea. *Journal of*
340 *Geophysical Research: Oceans*, 121(8), 5942-5958.

341
342 Chu, J. E., Lee, S. S., Timmermann, A., Wengel, C., Stuecker, M. F., & Yamaguchi, R. (2020).
343 Reduced tropical cyclone densities and ocean effects due to anthropogenic greenhouse warming.
344 *Science Advances*, 6(51), eabd5109.

345
346 Collins, T. W., Grineski, S. E., Chakraborty, J., & Flores, A. B. (2019). Environmental injustice
347 and hurricane harvey: A household-level study of socially disparate flood exposures in Greater
348 Houston, Texas, USA. *Environmental Research*, 179, 108772.

349
350 Dasgupta, P., Nam, S., Saranya, J. S., & Roxy, M. K. (2024). Marine heatwaves in the east asian
351 marginal seas facilitated by boreal summer intraseasonal oscillations. *Journal of Geophysical*
352 *Research: Oceans*, 129(2), e2023JC020602.

353
354 Data, Marine Meteorological. Ocean Data Standards.

355
356 Drennan, W. M., and L. K. Shay (2006), On the variability of the fluxes of momentum and sensible
357 heat, *Boundary Layer Meteorol.,* 119, 81–107.

Eich, M. L., Merrifield, M. A., & Alford, M. H. (2004). Structure and variability of semidiurnal internal tides in mamala bay, hawaii. *Journal of Geophysical Research: Oceans*, 109(C5).

Emanuel, K. A. (1986). An air-sea interaction theory for tropical cyclones. Part I: Steady-state maintenance. *Journal of Atmospheric Sciences*, 43(6), 585-605.

Emanuel, K. (2003). Tropical cyclones, *Annu. Rev. Earth Planet. Sci.*, 31, 75–104.

Emanuel, K. A. (2013). Downscaling CMIP5 climate models shows increased tropical cyclone activity over the 21st century. *Proceedings of the National Academy of Sciences*, 110(30), 12219-12224.

Gao, G., Marin, M., Feng, M., Yin, B., Yang, D., Feng, X., Ding, Y. and Song, D.,. (2020). Drivers of marine heatwaves in the east china sea and the south yellow sea in three consecutive summers during 2016–2018. *Journal of Geophysical Research: Oceans*, 125(8), e2020JC016518. https://doi.org/10.1029/2020JC016518

Gelaro, R., McCarty, W., Suarez, M. J., Todling, R., Molod, A., Takacs, L., Randlesm, C. A., Darmenov, A., Bosilovich, M. G., Reichle, R., Wargan, K., Coy, L., Cullather, R., Draper, C., Akella, S., Buchard, V., Conaty, A., Da Silva, A. M., Gu, W., Kim, G.-K., Koster, R., Lucchesi, R., Merkova, D., Nielsen, J. E., Partyka, G., Pawson, S., Putman, W., Rienecker, M., Schubert, S. D., Sienkiewicz, M., & Zhao, B. (2017). The Modern-era retrospective analysis for research and applications, version 2 (MERRA-2). *Journal of Climate*, 30(14), 5419–5454.

Gray, W. M. (1968). Global view of the origin of tropical disturbances and storms. *Mon. Wea. Rev.*, 96(10), 669-700.

Hobday, A. J., Alexander, L. V., Perkins, S. E., Smale, D. A., Straub, S. C., Oliver, E. C., Benthuysen, J. A., Burrows, M. T., Donat, M. G., Feng, M. and Holbrook, N. J., (2016). A hierarchical approach to defining marine heatwaves. *Progress in Oceanography*, 141, 227-238.

Holloway, P. E., Chatwin, P. G., & Craig, P. (2001). Internal tide observations from the australian north west shelf in summer 1995. *Journal of Physical Oceanography*, 31(5), 1182-1199.

Jacob, S. D., Shay, L. K., Mariano, A. J., & Black, P. G. (2000). The 3D oceanic mixed layer response to hurricane gilbert. *Journal of Physical Oceanography*, 30(6), 1407-1429.

Jaimes, B., Shay, L. K., & Brewster, J. K. (2016). Observed air-sea interactions in tropical cyclone isaac over loop current mesoscale eddy features. *Dynamics of Atmospheres and Oceans*, 76, 306-324.

Jaimes, B., Shay, L. K., & Uhlhorn, E. W. (2015). Enthalpy and momentum fluxes during hurricane earl relative to underlying ocean features. *Mon. Wea. Rev.*, 143(1), 111-131.

Jin, F. F., Boucharel, J., & Lin, I. I. (2014). Eastern pacific tropical cyclones intensified by El Niño delivery of subsurface ocean heat. *Nature*, 516(7529), 82-85.

Kang SK, Kim EJ, Kim S, Cione J, Lee D, Landwehr S, Kang H-W, Kim K-O, Hong CS, Kwon MH, Oh K-H, Lee JH, Noh S, So JK, Kang D-J, Kim D, Park J-H, Nam S, Cho YK, Ward B and Ginis I (2024) Anomalously large latent heat fluxes in low to moderate wind conditions within the eddy-rich zone of the Northwestern Pacific. *Front. Mar. Sci.* 11:1298641. doi: 10.3389/fmars.2024.1298641

Kawakami, Y., Nakano, H., Urakawa, L. S., Toyoda, T., Sakamoto, K., Yoshimura, H., Shindo, E. and Yamanaka, G., (2022). Interactions between ocean and successive typhoons in the kuroshio region in 2018 in atmosphere–ocean coupled model simulations. *Journal of Geophysical Research: Oceans*, 127(5), e2021JC018203.

Knauss, J. A., & Garfield, N. (2016). *Introduction to Physical Oceanography*. Waveland Press.

Knutson, T., Camargo, S.J., Chan, J.C., Emanuel, K., Ho, C.H., Kossin, J., Mohapatra, M., Satoh, M., Sugi, M., Walsh, K. & Wu, L., (2019). Tropical cyclones and climate change assessment: Part I: Detection and attribution. *Bulletin of the American Meteorological Society*, 100(10), 1987-2007.

Kunitsugu, M. (2012). Tropical cyclone information provided by the RSMC tokyo-typhoon center. *Tropical Cyclone Research and Review*, 1(1), 51-59.

Lee, S. W., & Nam, S. (2021). Estimation of propagation speed and direction of nonlinear internal waves from underway and moored measurements. *Journal of Marine Science and Engineering*, 9(10), 1089.

Lee, J. H., Lozovatsky, I., Jang, S. T., Jang, C. J., Hong, C. S., & Fernando, H. J. S. (2006). Episodes of nonlinear internal waves in the northern east china sea. *Geophysical Research Letters*, 33(18).

Lianshou, C., & Yihui, D. (1979). An Introduction to the western pacific typhoon. 1-491.

Lin, I. I., M. D. Chou, and C. C. Wu, (2011). The impact of a warm ocean eddy on typhoon morakot: A preliminary study from satellite observations and numerical modelling. *TAO: Terrestrial, Atmospheric and Oceanic Sciences*, 22, 661-671, doi: 10.3319/TAO.2011.08.19.01(TM)

C. C., Chan, J. C., & Toumi, R. (2021). Tropical cyclones near landfall can induce their own intensification through feedbacks on radiative forcing. *Communications Earth & Environment*, 2(1), 1–10. https://doi.org/10.1038/s43247-021-00259-8

Malkus, J. S., and H. Riehl (1960), On the dynamics and energy transformations in steady state hurricanes, *Tellus*, 12(1), 1–20.

M MA (2024). lsf (https://www.mathworks.com/matlabcentral/fileexchange/8707-lsf), MATLAB Central File Exchange. Retrieved February 1, 2024.

Murakami, H., Delworth, T. L., Cooke, W. F., Zhao, M., Xiang, B., & Hsu, P. C. (2020). Detected climatic change in global distribution of tropical cyclones. *Proceedings of the National Academy of Sciences*, 117(20), 10706-10714.

Nam, S., Kim, D. J., Lee, S. W., Kim, B. G., Kang, K. M., & Cho, Y. K. (2018). Nonlinear internal wave spirals in the northern east china sea. *Scientific Reports*, 8(1), 3473.

Nam, S., Kim, D. J., & Moon, W. M. (2012). Observed impact of mesoscale circulation on oceanic response to typhoon Man-Yi (2007). *Ocean Dynamics*, 62, 1-12.

NOAA National Centers for Environmental Information. (2022). ETOPO 2022 15 arc-second global relief model.

Oppenheimer, M., Glavovic, B., Hinkel, J., van de Wal, R., Magnan, A. K., Abd-Elgawad, M., Cai, R., Cifuentes-Jara, M., Deconto, R.M., Ghosh, T. and Hay, J., (2019). Sea level rise and implications for low-lying islands, coasts and communities. In H.-O. Pörtner, et al. (Eds.), *Special report on the ocean and cryosphere in a changing climate.*. IPCC. Retrieved from https://www.ipcc.ch/srocc/chapter/chapter-4-sea-level-rise-and-implications-for-low-lying-islands-coasts-and-communities/

Park, J. H., Yeo, D. E., Lee, K., Lee, H., Lee, S. W., Noh, S., Kim, S., Shin, J., Choi, Y. &Nam, S., (2019). Rapid decay of slowly moving typhoon soulik (2018) due to interactions with the strongly stratified northern east china sea. *Geophysical Research Letters*, 46(24), 14595-14603.

Pawlowicz, R., Beardsley, B., & Lentz, S. (2002). Classical tidal harmonic analysis including error estimates in MATLAB using T_TIDE. *Computers & Geosciences*, 28(8), 929-937.

Pun, I. F., Hsu, H. H., Moon, I. J., Lin, I. I., & Jeong, J. Y. (2023). Marine heatwave as a supercharger for the strongest typhoon in the east china sea. *npj Climate and Atmospheric Science*, 6(1), 128.

Rathore, S., Goyal, R., Jangir, B., Ummenhofer, C. C., Feng, M., & Mishra, M. (2022). Interactions between a marine heatwave and tropical cyclone amphan in the bay of bengal in 2020. *Frontiers in Climate*, 4, 861477.

Reynolds, R. W., Smith, T. M., Liu, C., Chelton, D. B., Casey, K. S., & Schlax, M. G. (2007). Daily high-resolution-blended analyses for sea surface temperature. *Journal of Climate*, *20*(22), 5473-5496.

Saranya, J. S., Roxy, M. K., Dasgupta, P., & Anand, A. (2022). Genesis and trends in marine heatwaves over the tropical indian ocean and their interaction with the indian summer monsoon. *Journal of Geophysical Research: Oceans*, 127(2), e2021JC017427.

Saranya, J. S., & Nam, S. (2024). Subsurface evolution of three types of surface marine heatwaves over the east sea (japan sea). *Progress in Oceanography*, 103226.

Shay, L. K., Goni, G. J., & Black, P. G. (2000). Effects of a warm oceanic feature on hurricane opal. *Monthly Weather Review*, 128(5), 1366-1383.

Shay, L. K., & Uhlhorn, E. W. (2008). Loop current response to hurricanes isidore and lili. *Monthly weather review*, 136(9), 3248-3274.

Wada, A., Uehara, T., & Ishizaki, S. (2014). Typhoon-induced sea surface cooling during the 2011 and 2012 typhoon seasons: Observational evidence and numerical investigations of the sea surface cooling effect using typhoon simulations. *Progress in Earth and Planetary Science*, 1, 1-25.

Webster, P. J., Holland, G. J., Curry, J. A., & Chang, H. R. (2005). Changes in tropical cyclone number, duration, and intensity in a warming environment. *Science*, 309(5742), 1844-1846.

Xu, Z., Liu, K., Yin, B., Zhao, Z., Wang, Y., & Li, Q. (2016). Long-range propagation and associated variability of internal tides in the south china sea. *Journal of Geophysical Research: Oceans*, 121(11), 8268-8286.

Yan, Z., Ding, Y., Zhai, P., Song, L., Cao, L., & Li, Z. (2020). Re-assessing climatic warming in china since 1900. *Journal of Meteorological Research*, 34(2), 243-251.

Zhang, J. A., Black, P. G., French, J. R., & Drennan, W. M. (2008). First direct measurements of enthalpy flux in the hurricane boundary layer: The CBLAST results. *Geophysical research letters*, 35(14).

Zhao, Z. (2014). Internal tide radiation from the luzon strait. *Journal of Geophysical Research: Oceans*, 119, 5434–5448.

Zhao, Z. (2020). Southward internal tides in the northeastern south china sea. *Journal of Geophysical Research: Oceans*, 125(11), e2020JC016554.

Zheng, Z. W., Ho, C. R., Zheng, Q., Lo, Y. T., Kuo, N. J., & Gopalakrishnan, G. (2010). Effects of preexisting cyclonic eddies on upper ocean responses to Category 5 typhoons in the western north pacific. *Journal of Geophysical Research: Oceans*, 115(C9).
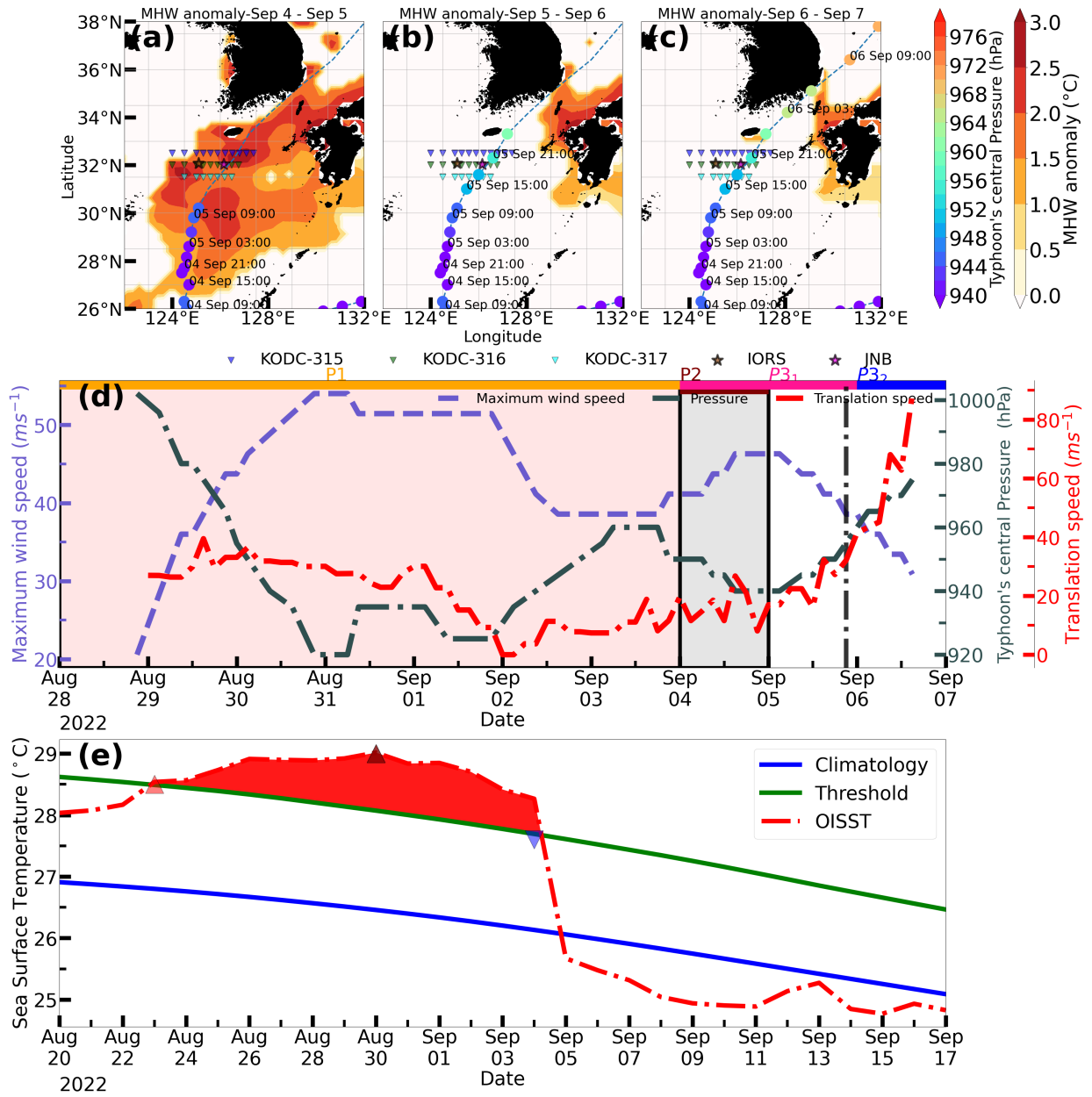
Figure 1. (a, b, c) MHW anomalies, overlaid with typhoon Hinnamnor's track and central pressure (Stars represent in-situ observations from I-ORS (brown) and JNB (magenta) and traingles represent ship-board hydrographic observations along Lines 315 (blue), 316 (green), and 317(cyan). (d) Timeseries of maximum wind speed (m s⁻¹), typhoon's central pressure (hPa), and translation speed (m s⁻¹). The red and grey-shaded intervals represent the MHW and interaction between MHW-typhoon periods. The dotted vertical line represents the time step with maximum typhoon winds at I-ORS. The orange, brown, pink, and blue timelines on the top represent the

539   different stages of MHW-typhoon interactions. (e) Timeseries of OISST representing MHW at the

540   I-ORS location (start, peak and end dates)
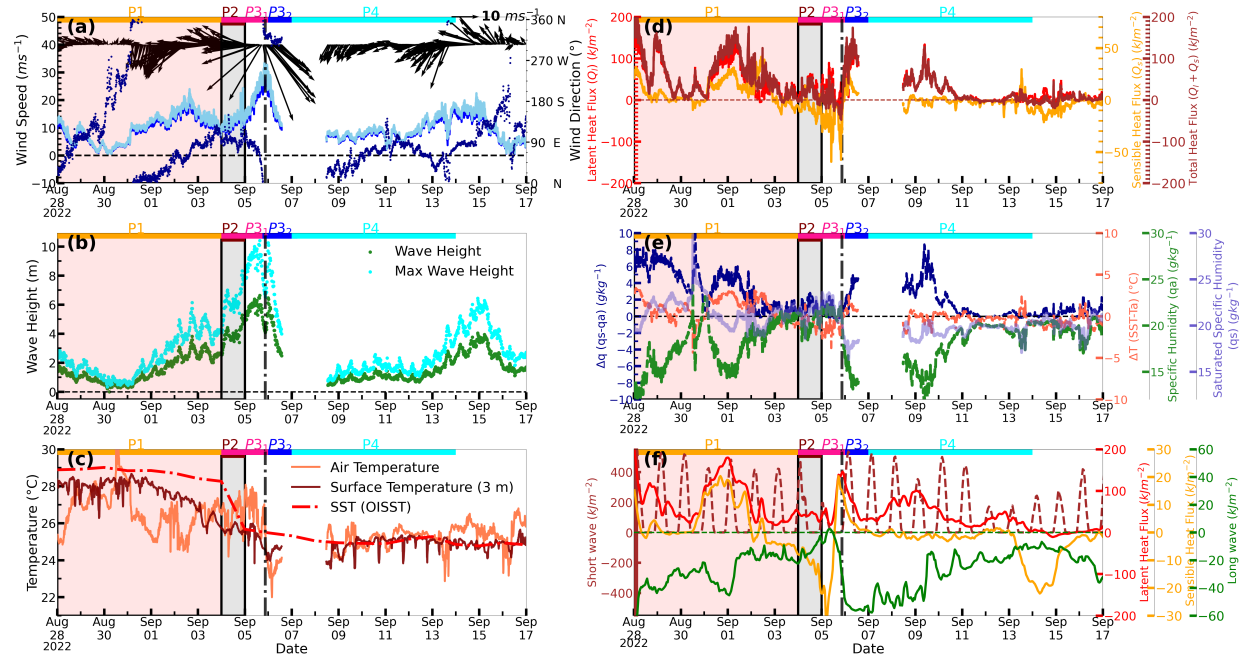
541

542

543   **Figure 2**. I-ORS timeseries observations (a) wind speed (m s^{-1}), wind gust (m s^{-1}), and wind

544   direction (measured clockwise direction from the north). (b) Wave height (m) and maximum wave

545   height (m). (c) Air temperature (˚C), temperature at 3 m (˚C), and OISST (˚C). (d) Latent heat

546   flux, sensible heat flux, and total heat flux (kJ m^{-2}). (e) Δq ($q_s - q_a$) (g kg^{-1}), ΔT (SST $- T_a$) (˚C),

547   q_s (g kg^{-1}), and q_a (g kg^{-1}). (f) Shortwave, latent heat flux, sensible heat flux, and longwave (kJ

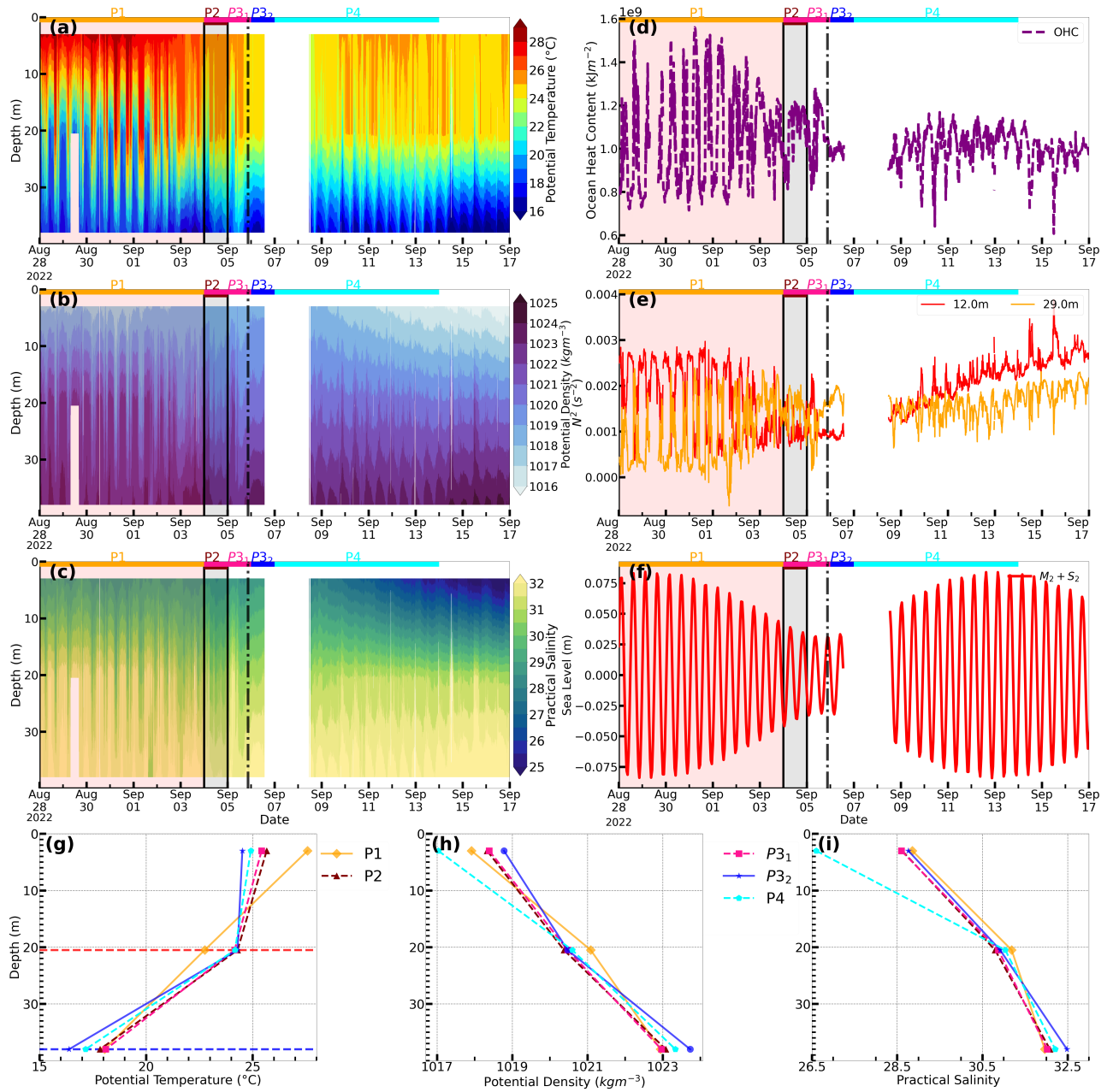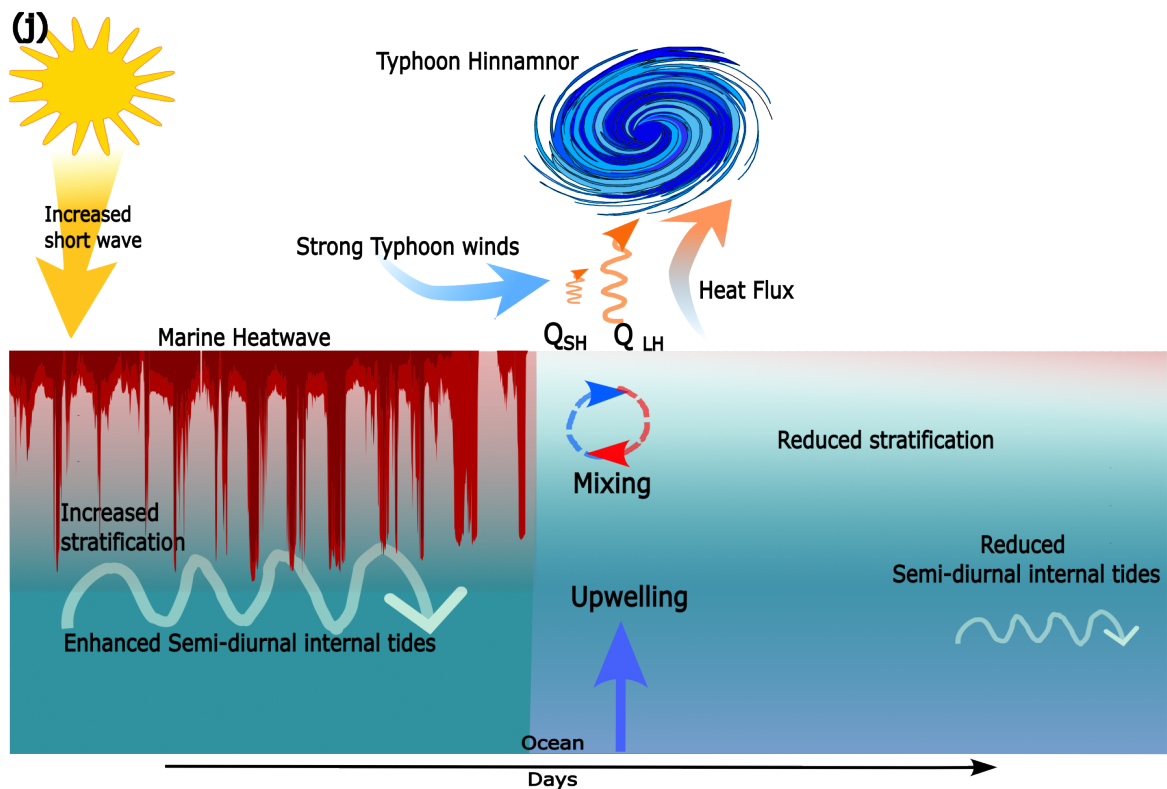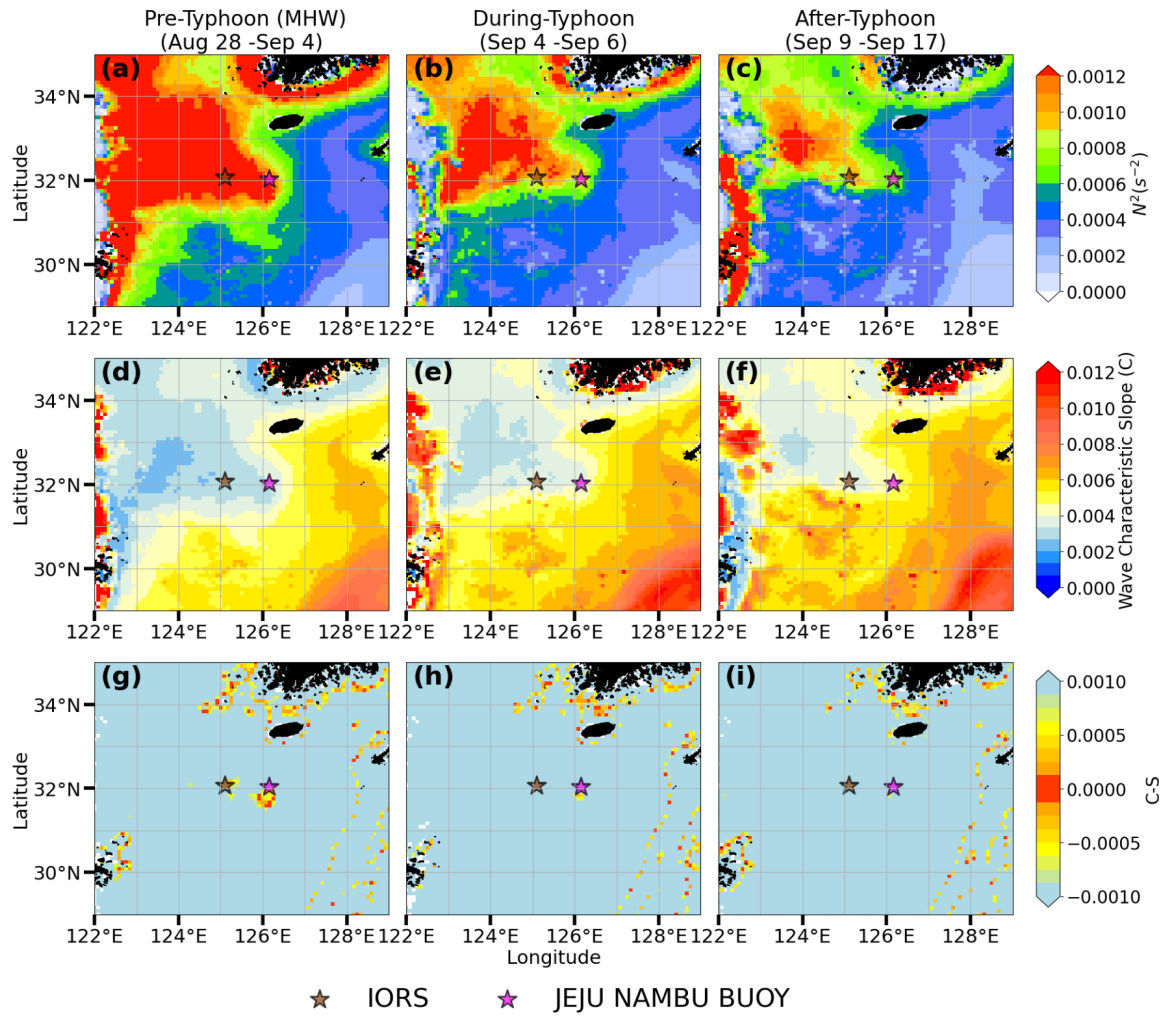548   m^{-2}) (MERRA-2 datasets). The shaded intervals, dotted line and timelines on the top are same as

549   Figure 1.

550

Figure 3. Time-depth plot of (a) potential temperature (˚C), (b) potential density (kg m⁻³), and (c) practical salinity (psu). Timeseries of (d) OHC (kJ m⁻²), (e) N^2 (s⁻²), (f) M_2 and S_2 components of sealevel. Mean vertical profiles of (g) potential temperature (with MLD in m before and after the

555   typhoon passage denoted by red and blue), (h) potential density, and (i) practical salinity in the
556   different stages of MHW-typhoon interactions.

557

★ IORS   ★ JEJU NAMBU BUOY

558

Figure 4. Spatial distribution of (a-c) N^2 (s^{-2}). (d-f) wave characteristic slope (C). (g-i) difference between wave characteristic slope (C) and bottom slope (S) (C-S). The star symbols are the locations of I-ORS (brown) and JNB (magenta). (j) Schematic representation of interaction between MHW, ITs and typhoon Hinnamnor at I-ORS location.

563
564
565
566